RSC Advances

PAPER

View Article Online
View Journal | View Issue

Cite this: *RSC Adv.*, 2026, **16**, 24406

Nanoconfinement-enabled GO hydrogels *via* Hummers' method for real-time health monitoring

Lili Tian, *[a] Zhiming Yang*[ab] and Qin Wang*[ab]

Traditional hydrogels fail to meet the stringent requirements of flexible electronics and biomedical engineering due to their inherent performance limitations. Herein, graphene oxide (GO) was synthesized *via* the Hummers' method, and nanoconfinement-enabled GO nanocomposite hydrogels were fabricated by incorporating GO into a borate ester crosslinking network. Dynamic borate bonds synergistically interact with the surface functional groups of GO to enhance the mechanical properties of the hydrogels, while the lamellar structure of GO effectively disperses stress and suppresses crack propagation. The as-fabricated hydrogel exhibits remarkable tensile strength (161 kPa), elongation at break (938%), high self-healing efficiency (89.1% for strength and 83.1% for strain), and superior fatigue resistance (recovery rate >90% after cyclic tensile and compressive tests). The hydrogel-based sensor demonstrates tunable gauge factors (1.7 within the 0–250% strain range and 5.3 within the 250–300% strain range), a rapid response time (240 ms), and stable cyclic performance (1000 consecutive cycles at 150% strain). This sensor can precisely monitor various human movements, including joint motion, finger bending, and vocal cord activity, thereby providing a promising platform for real-time intelligent personal health monitoring.

Received 25th February 2026
Accepted 3rd May 2026

DOI: 10.1039/d6ra01645f

rsc.li/rsc-advances

1 Introduction

Hydrogel materials with mechanical properties, self-healing capabilities, and intelligent response characteristics have become the core carrier of next-generation wearable devices and implantable sensors with the deep integration of flexible electronics technology and biomedical engineering.[1,2] However, traditional hydrogels have insufficient mechanical strength due to the disordered distribution of polymer chains, and their chemical cross-linking structures are difficult to self-repair after being damaged, which severely limits their long-term stability in dynamic biological environments.[3,4] In recent years, breakthroughs in nanoconfinement effects and biomimetic self-assembly strategies have provided new insights into resolving this contradiction.[5–7] By constructing two-dimensional nanomaterials into ordered confined spaces, polymer chains can be precisely entangled, thereby enhancing rigidity while retaining molecular chain dynamics, thus overcoming the inherent contradiction between "high strength" and "self-healing."[8,9]

Graphene oxide (GO) is a two-dimensional nanomaterial with excellent mechanical properties, conductivity, and biocompatibility.[10–12] Its surface is rich in hydroxyl, carboxyl, and epoxy groups, which not only give it excellent hydrophilicity and dispersibility, but also enable it to form dynamic cross-linked networks with polymer chains through noncovalent interactions such as hydrogen bonds and π–π stacking.[13,14] These interactions can enhance the mechanical properties of hydrogels through physical or chemical cross-linking. In addition, GO nanosheets prepared based on the Hummers' method have a single-layer structure and high aspect ratio characteristics. The interlayer spacing can be precisely controlled to the range of 1–10 nm through ultrasonic exfoliation, providing an ideal building block for constructing nanoscale confined spaces.[15,16] The layered structure of graphene oxide can also effectively disperse stress, inhibit crack propagation, and further enhance the toughness of the material.[17,18]

Materials used in the field of smart health monitoring must possess high sensitivity, a wide detection range, and stability in dynamic environments.[19,20] However, traditional hydrogel sensors generally suffer from low sensitivity and poor durability, making them unsuitable for long-term stable monitoring.[21–23] For example, ion-conductive hydrogels, while highly stretchable, are susceptible to changes in environmental humidity and may suffer irreversible damage after repeated stretching.[24,25] In contrast, integrating the confined structure of graphene oxide (GO) with the dynamic cross-linking network of boronate ester bonds enables the construction of an intelligent sensing platform that combines high strength and high sensitivity.[26,27] When microcracks form in the material under external force, the dynamic bonds within the nanoconfined

[a]*Ningxia Key Laboratory of Green Catalytic Materials and Technology, College of Chemistry and Chemical Engineering, Ningxia Normal University, Guyuan 756099, China. E-mail: tianlili@nxnu.edu.cn; yangzhiming1978@163.com; nxwangqin2018@163.com*

[b]*Key Laboratory of Soil Ecological Health and Microbial Regulation, School of Resources, Environment and Life Sciences, Ningxia Normal University, Guyuan, 756009, China*

space rapidly reorganize to achieve self-healing.[28–30] Meanwhile, the conductivity enhancement effect of GO allows for precise capture of conductivity changes caused by crack propagation, facilitating the preparation of hydrogel sensors with both high sensitivity and self-healing capabilities.[31–33] This makes real-time monitoring of physiological parameters such as joint movements and myocardial electrical signals feasible.[34,35] Additionally, self-healing through bond cleavage and reorganization significantly enhances the material's cyclic stability. Such sensors exhibit immense potential in fields such as human motion monitoring, human–machine interaction interfaces, and soft robotics, providing data support for rehabilitation training or motion analysis by enabling real-time monitoring of joint flexion angles or muscle contraction forces.[36,37]

In the design of self-healing mechanisms, the synergistic interaction between dynamic covalent bonds and non-covalent bonds has emerged as a key breakthrough.[38,39] However, existing research still faces challenges. For example, while the dynamic properties of borate ester bonds confer self-healing capabilities to materials, their low bond energy may lead to reduced stability in high-temperature or high-humidity environments. Additionally, the dispersion of graphene oxide and its interfacial interactions with polymers require further optimization to prevent performance degradation caused by agglomeration. To address these issues, this study proposes the incorporation of graphene oxide into a borate ester-crosslinked hydrogel system. By regulating the crosslinking density of borate ester bonds and the concentration of graphene oxide, a graphene oxide hydrogel with high strength, self-healing, and sensing functions is constructed. The core of this strategy lies in utilizing the electrostatic repulsion between nanoplates to spontaneously form coplanar arrangements, enabling polymer chains to form dense entanglements within a confined space. This approach enhances rigidity through physical confinement while preserving self-healing capabilities through dynamic bond reorganization. Specifically, GO was successfully synthesized using the Hummers' method and then uniformly dispersed in the polymer matrix through *in situ* polymerization. A multi-crosslinked network was formed through the synergistic action of borate ester bonds and hydrogen bonds. By optimizing the formulation and process parameters, a balance was achieved between the material's mechanical properties, self-healing efficiency, and sensing sensitivity. This study aims to systematically investigate the synergistic mechanism between borate ester bonds and nano-confined self-assembly, revealing their influence on the mechanical properties, self-healing ability, and sensing characteristics of hydrogels. By regulating the crosslinking density of borate ester bonds and the content of graphene oxide, a hydrogel sensor with high strength (tensile stress ≥161 kpa), rapid self-healing (healing efficiency ≥89%), high sensitivity (strain GF ≥5), and fast response (time of 240 ms) is prepared, demonstrating flexible application potential in human motion monitoring. This study provides a material foundation for developing the next generation of flexible electronic devices and theoretical support for the application of dynamic covalent bonds in smart materials. The borate ester-based high-strength self-healing graphene oxide hydrogel sensor developed in this study is expected to promote the widespread application of flexible electronic technology in multiple fields.

2 Results and discussion

2.1 Design and synthesis of multifunctional nanocomposite hydrogels

To design a GO-enhanced nanocomposite hydrogel, graphene oxide was first prepared based on the Hummers' method,[40] as shown in Fig. 1A. The prepared GO was used as a nano-reinforcing agent, and the nanoconfinement self-assembly composite hydrogel was successfully synthesized by radical polymerization (Fig. 1B). By adopting specific strategies, the borate ester bonds formed between the hydroxyl groups on (PVA) and the boric acid groups on 3-acrylamidophenylboronic acid (AAPBA), as well as the hydrogen bonds between the amino groups on acrylamide (AM) and the hydroxyl groups on PVA and the amino groups on AAPBA, are utilized. Additionally, by assembling two-dimensional nanomaterials into ordered confined structures, polymer chains can be arranged into a finely ordered entangled state. This structure enhances the rigidity of the material while maintaining the dynamic properties of the polymer molecular chains, thereby resolving the inherent contradiction between "high strength" and "self-healing" properties that is difficult to reconcile. The chemical structure, along with the chemical bonds are depicted in Fig. 1C, which involves multiple dynamic borate ester bonds and hydrogen bonds.

2.2 Structure and morphology analysis

The chemical composition of the hydrogel was characterized by Fourier transform infrared spectroscopy (FTIR). The peak at 1120 cm^{-1} is attributed to the characteristic absorption of the B–O–C bond in the borate ester structure. As shown in Fig. 1D, the $A_{35}P_5B_{17.5}M_{15}$–$GO_{1.5}$ hydrogel exhibits enhanced C–H bond absorption peaks at 3346 cm^{-1} and in the 1600–1647 cm^{-1} region, which is attributed to the formation of numerous hydrogen bonds between GO and the polymer chains. Although the addition of GO enhances hydrogen bonding interactions, it does not significantly affect the characteristic peak of the borate ester structure at 1120 cm^{-1}.

The scanning electron microscopy (SEM) image of the as-prepared graphene oxide (GO) is presented in Fig. S1, as shown in the SEM micrograph, GO presents a typical layered and wrinkled sheet structure. The GO nanosheets exhibit a crumpled and folded morphology with abundant surface ripples and folds, which are formed to minimize the surface energy of the 2D structure. The randomly distributed wrinkles and overlapping sheet edges further confirm the successful exfoliation of GO, while maintaining a thin, flexible lamellar structure. These structural features also help to inhibit the aggregation and restacking of GO sheets, which is beneficial for the subsequent fabrication of composite materials. The hydrogel was rapidly quenched with liquid nitrogen, dried in a freeze dryer for 24 hours, and a gold layer was further sputter-coated

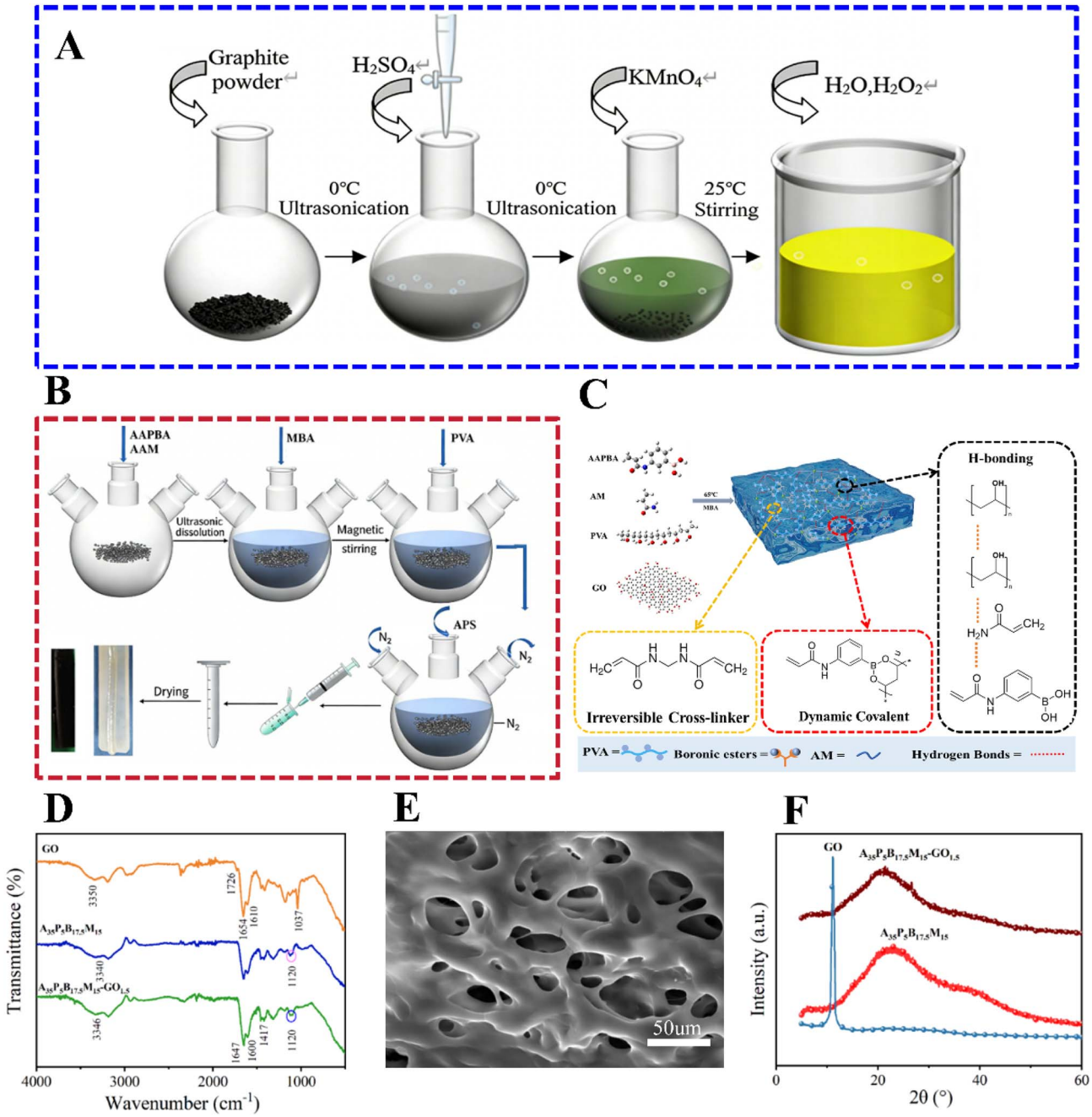

Fig. 1 Structure and properties of nanocomposite hydrogels, (A) preparation of GO and (B) nanocomposite hydrogels, (C) multiple dynamic interactions of nanocomposite hydrogels, (D) FTIR spectra of the GO and hydrogels, (E) SEM image of the $A_{35}P_5B_{17.5}M_{15}$–$GO_{1.5}$ hydrogel, scale bar: 50, (F) XRD patterns of the GO and hydrogel.

on the cross-section of the hydrogel for 120 seconds. A scanning electron microscope (SEM, ZEISS SIGMA, Germany) was used to observe the morphology and internal structure of the hydrogel, as depicted in Fig. 1E (Fig. S2A). The nanocomposite hydrogel exhibited a three-dimensional (3D) porous network structure, indicating that the uniform dispersion of graphene oxide (GO) as a nano-reinforcing agent within the hydrogel network had no adverse impact on its structural integrity. X-ray diffraction (XRD) (Fig. 1F) shows that GO has a distinct diffraction peak at 10.64°, while the $A_{35}P_5B_{17.5}M_{15}$ and $A_{35}P_5B_{17.5}M_{15}$–$GO_{1.5}$ hydrogels have a distinct diffraction peak at 23.6°, not at 10.64°. This indicates that GO is well dispersed in the nanogel and forms hydrogen bonds with other monomers.

2.3 Optimization of the hydrogel synthesis process, establishment of the response surface model, and analysis of the significance of the regression equation

To systematically assess the mechanism by which monomer concentration influences the mechanical properties of hydrogel, this study conducted an in-depth analysis of key

mechanical parameters such as tensile strength, fracture strain, elastic modulus, and toughness based on stress–strain curve testing.

The relevant test results are detailed in Fig. 2. By precisely controlling the concentration of polyvinyl alcohol (PVA) (Fig. 2A–C) and the content of 3-acrylamidobenzoic acid (AAPBA) (Fig. 2D–F), acrylamide (AM) (Fig. 2G–I), and *N*,*N*′-methylenebisacrylamide (MBA) (Fig. 2J–L), the hydrogel samples were optimized through design. It was ultimately found that when the preparation process parameters were set as follows: AM concentration 35 wt%, PVA concentration of 5 wt%, AAPBA content of 17.5 mg mL^{-1}, and MBA concentration of 15 wt%, the resulting $A_{35}P_5B_{17.5}M_{15}$ hydrogel exhibited outstanding properties in terms of tensile strength, toughness, and overall mechanical performance, demonstrating both high strength and self-healing capability.

Using Design Expert 13 software,[41] analyze the single-factor experimental data in Fig. 3 and 4 and establish a multiple regression model. The stress–strain response surfaces are shown in Fig. 3 and 4. The stress quadratic polynomial regression equations obtained for different monomer concentrations are as follows:

$$\text{Stress} = 96.42 + 0.54a - 0.08b + 0.17c - 018d + 0.98ab - 1.15ac - 0.45bc - 0.63bd + 0.65cd - 0.89a^2 - 1.83b^2 - 1.00c^2 - 1.04d^2$$

$$\text{Strain} = 413.2 - 0.58a + 1.50b + 0.42c - 0.50d + 0.75ab - 0.75ac - 0.25ad + 0.75bd - 1.00cd - 8.39a^2 - 9.52b^2 - 8.64c^2 - 7.52d^2$$

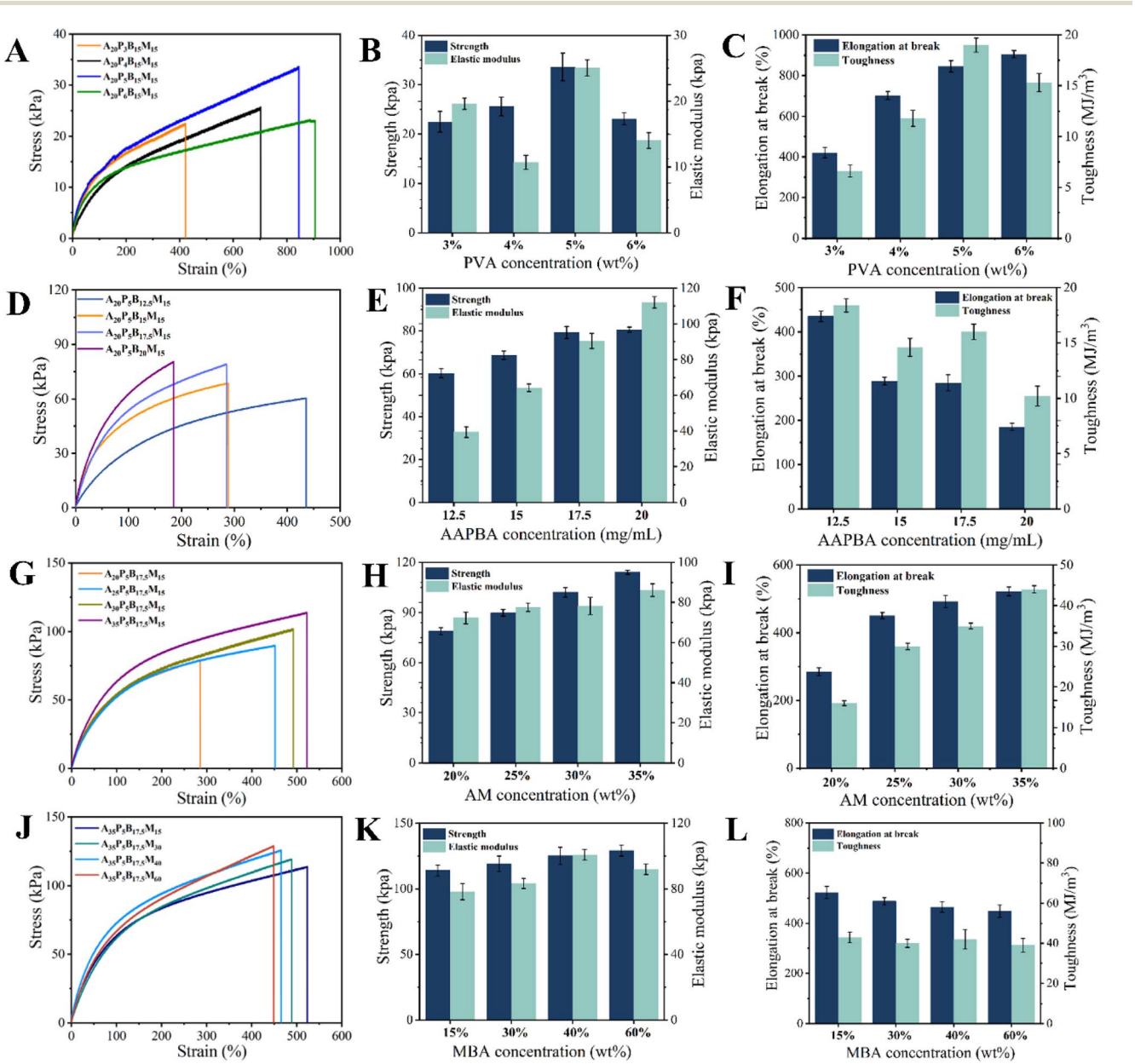

Fig. 2 The stress–strain with different monomer content, (A) PVA, (D) AAPBA, (G) AM, and (J) MBA, (B), (E), (H) and (K) fracture strength and elasticity modulus, (C), (F), (I) and (L) elongation at break and toughness.

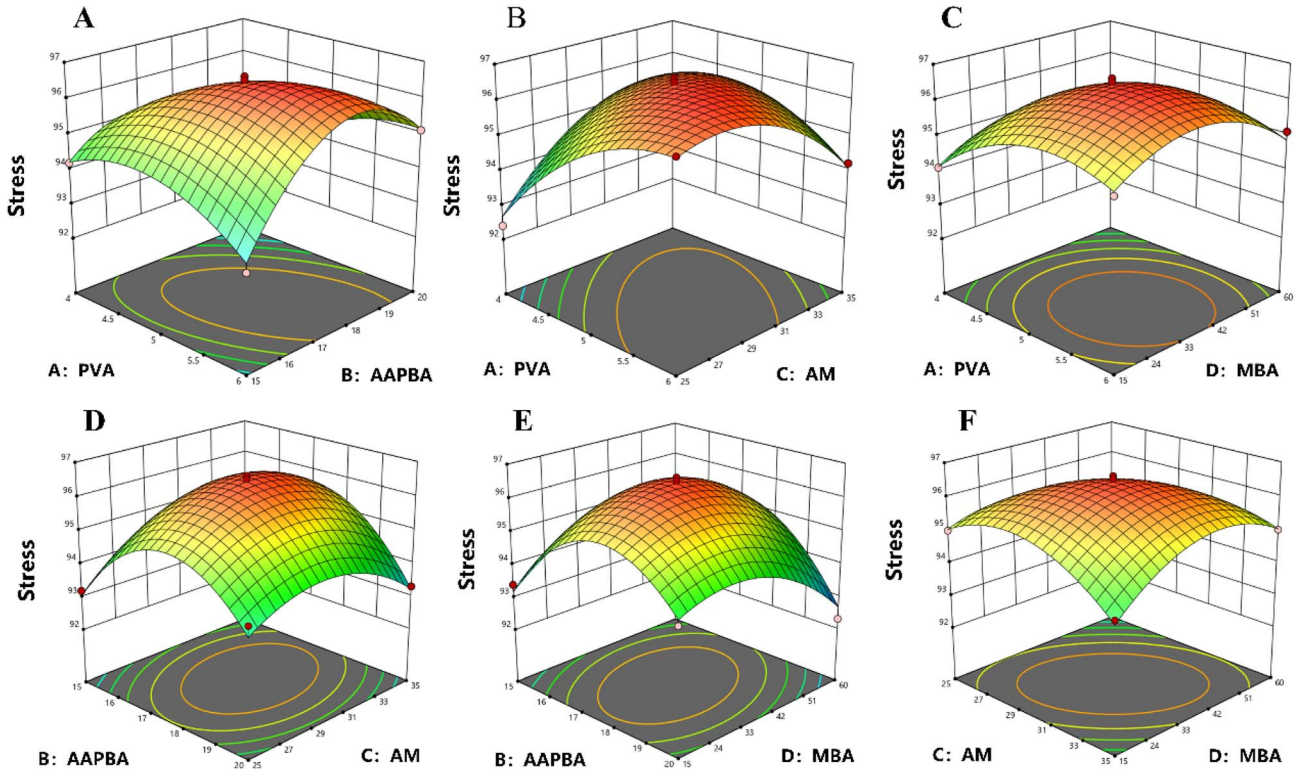

Fig. 3 The interaction between the variables on the response value stress, (A) PVA and AAPBA, (B) PVA and AM, (C) PVA and MBA, (D) AAPBA and AM, (E) AAPBA and MBA, (F) AM and MBA.

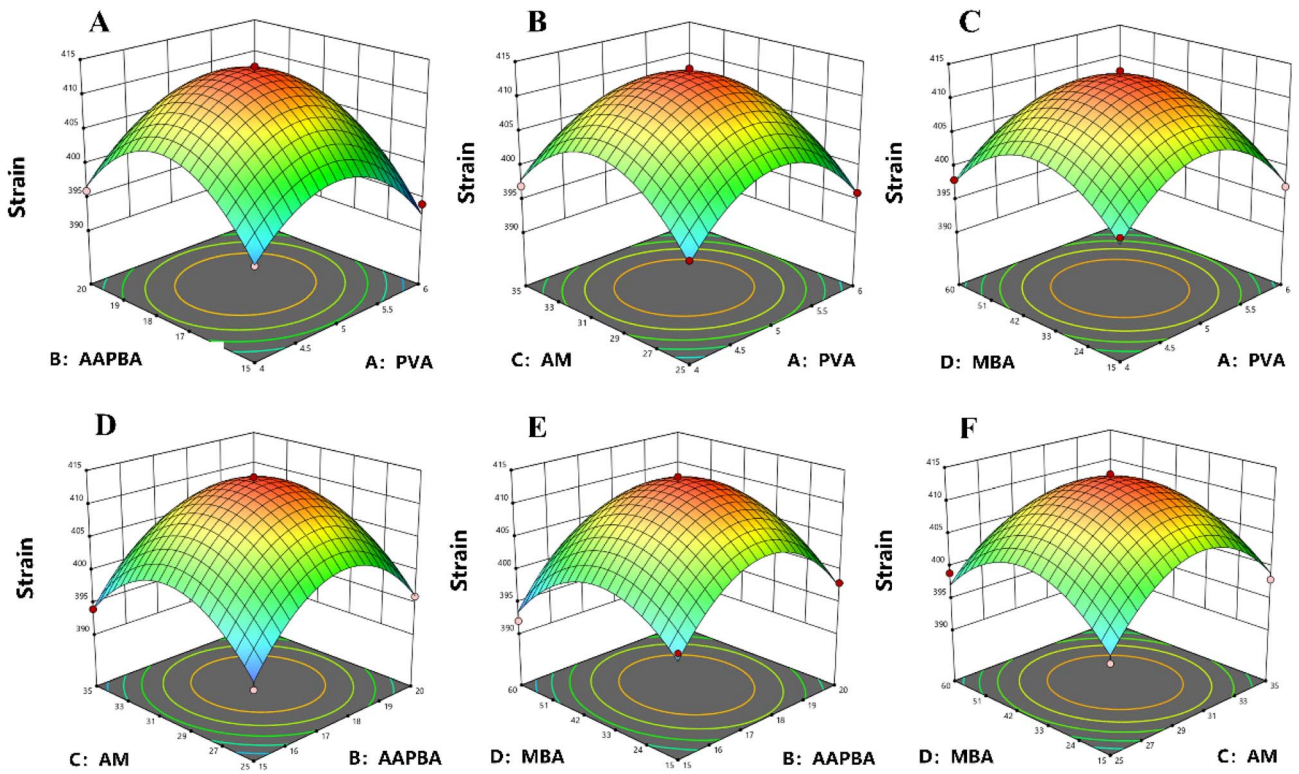

Fig. 4 The interaction between the variables on the response value strain, (A) PVA and AAPBA, (B) PVA and AM, (C) PVA and MBA, (D) AAPBA and AM, (E) AAPBA and MBA, (F) AM and MBA.

The results show that the stress model has $F = 3.66$ and $P = 0.0001 < 0.05$, indicating that the model is significantly different. R is 0.9806, indicating that the equation matches the corresponding response values to a degree of 98.06%. The results show that the strain model has $F = 3.99$ and $P = 0.0001 < 0.05$, indicating that the model is significantly different. R is 0.9763, indicating that the equation matches the corresponding response values to a degree of 97.63%. Additionally, the F-test revealed that the primary and secondary factors influencing stress are the quality of Additionally, the F-test revealed that the primary and secondary factors influencing stress are the quality of MBA > PVA > AAPBA > AM content. This is completely consistent with the formation of covalent bonds in composite hydrogels (PVA forms borate bonds with AAPBA, and MBA is a chemical cross-linking agent that forms irreversible covalent bonds, which are strong but irreversible).

The $A_{35}P_5B_{17.5}M_{15}$ hydrogel fabricated under the optimal preparation protocol exhibited superior self-healing capacity and mechanical performance. After a circular hydrogel sample was sliced with a blade, the fresh fractured surfaces were brought into immediate contact. Following self-healing at room temperature, the hydrogel was capable of withstanding various deformations, including stretching, squeezing, compression, and knotting, as illustrated in Fig. S3. Upon removal of the applied finger pressure, the $A_{35}P_5B_{17.5}M_{15}$ hydrogel instantly recovered its original shape, demonstrating excellent elasticity and self-recovery properties.

2.4 Mechanical and fatigue resistance

The mechanical performance of the nano-composite hydrogel was further improved when GO was used as a secondary cross-linking point, and a hierarchical reversible cross-linking network was established, digital photographs of hydrogels with different GO contents are displayed in Fig. S3E.The mechanical properties of the hydrogels were evaluated through tensile experiments, with key parameters analyzed. Fig. 5A illustrates the testing results of the $A_{35}P_5B_{17.5}M_{15}GO_n$ hydrogel samples. The fracture stress and strain of $A_{35}P_5B_{17.5}M_{15}GO_{0.5}$ were enhanced compared to those of $A_{35}P_5B_{17.5}M_{15}GO_0$. As the GO content increased, the fracture stress rose, which was attributed to the van der Waals forces and hydrogen bonding interactions between GO and the network. The tensile strength of $A_{35}P_5B_{17.5}M_{15}GO_2$ was 1.43 times that of $A_{35}P_5B_{17.5}M_{15}GO_0$. Fig. 5B indicates that the stiffness of the hydrogels increased with the rising GO content, with $A_{35}P_5B_{17.5}M_{15}GO_2$ exhibiting the highest elastic modulus. This was due to the formation of more hydrogen bonds within the hydrogel, leading to a higher crosslinking density and a more compact network structure. Fig. 5C reveals that the toughness of the hydrogels initially increased and then decreased with an increase in GO content.

When the GO content ranged from 0.5 wt% to 1.5 wt%, the toughness of $A_{35}P_5B_{17.5}M_{15}GO_{0.5}$, $A_{35}P_5B_{17.5}M_{15}GO_1$, and $A_{35}P_5B_{17.5}M_{15}GO_{1.5}$ improved significantly, reaching 66.93, 77.77, and 107.60 MJ m^{-3}, respectively, which were notably higher than the 53.79 MJ m^{-3} of $A_{35}P_5B_{17.5}M_{15}GO_0$. However, when the GO content increased to 2 wt%, the toughness of the hydrogel decreased. This was because the high GO content resulted in an increased total number of hydrogen bonds and enhanced crosslinking density within the hydrogel, causing a significant decline in the elongation at break when resisting external forces. Consequently, despite the possible enhancement of local strength due to the increased hydrogen bonds, the decrease in elongation at break led to an overall reduction in the toughness of the hydrogel. GO nanosheets prepared using the Hummers' method have a single-layer structure and high aspect ratio characteristics. The interlayer spacing can be precisely controlled to a range of 1–10 nm through ultrasonic exfoliation, providing an ideal building block for constructing nanoscale confined spaces. The layered structure of graphene oxide can also effectively disperse stress and inhibit crack propagation, further enhancing the toughness of the material.

Anti-fatigue performance tests were conducted on $A_{35}P_5B_{17.5}M_{15}GO_{1.5}$ hydrogel as shown in Fig. 5D–F. Its elasticity and recovery were assessed *via* continuous cyclic tensile tests without intervals: it was stretched to 100%, 200%, and 500% strain at 100 mm min^{-1} and then recovered at the same rate, with the cycle repeated 10 times (stress–time plots in Fig. S4A–C). Although stress decreased in the second cycle compared to the first, the stress–strain curves from cycles 2 to 10 almost completely overlapped, and the peak stress recovery rate remained around 94% after 10 cycles, indicating excellent resilience and anti-fatigue performance.

The cylindrical $A_{35}P_5B_{17.5}M_{15}GO_{1.5}$ hydrogel exhibited no fracture under a high compressive strain of up to 90% and rapidly restored its initial shape after load release, as shown in Fig. 5G. Over the subsequent 10 cycles, its recovery rate remained above 90% of the peak stress, demonstrating exceptional compressive elasticity. During large deformations, the borate ester bonds between hydrogel molecular chains and the multiple hydrogen bonds between GO and molecules underwent rapid cleavage and reassociation, enabling effective energy dissipation. This mechanism allowed the $A_{35}P_5B_{17.5}M_{15}GO_{1.5}$ hydrogel to swiftly recover its original shape upon removal of external forces, showcasing superior elasticity and self-healing properties.

2.5 Rheological behavior and self-healing property

The rheological properties of the $A_{35}P_5B_{17.5}M_{15}GO_{1.5}$ hydrogel were characterized. As shown in Fig. 5H, within the angular frequency range of 0.1–100 rad s^{-1}, the storage modulus (G') of the hydrogel consistently remained higher than the loss modulus (G''), indicating the formation of a stable cross-linked network and exhibiting distinct elastic characteristics. To determine the linear viscoelastic region, measurements were conducted within the strain range of 0.1–1000% at a fixed angular frequency of 10 rad s^{-1} (Fig. 5I). It was observed that both G' and G'' remained relatively stable until the strain reached 150%. As the strain continued to increase, G' and G'' intersected at a strain of 234%, which marked the disruption of the internal network of the hydrogel under large strains.

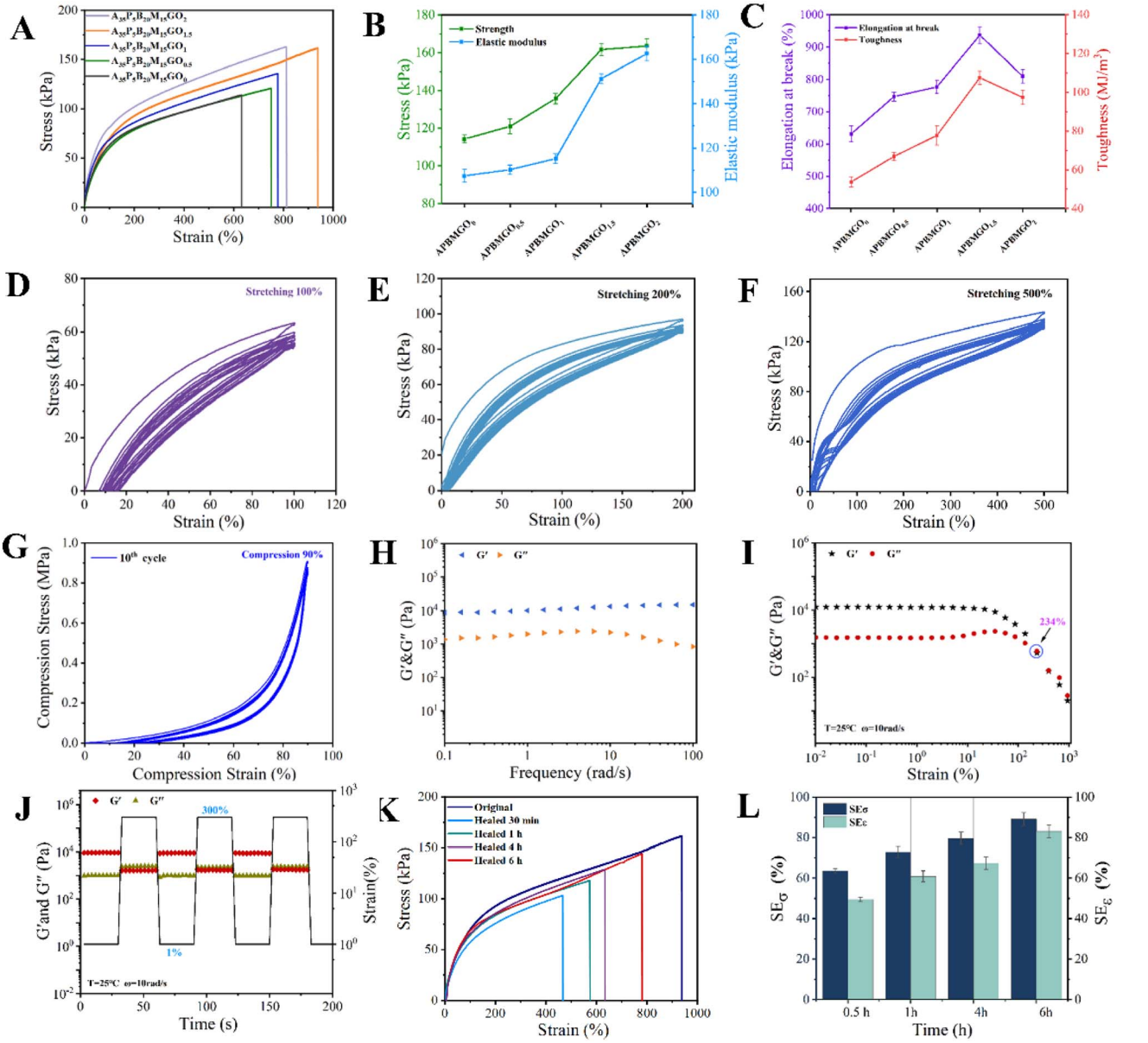

Fig. 5 The APBM with different contents of GO, (A) tensile stress–strain curves, (B) tensile strength and Young's modulus, (C) elongation at break and toughness, cycles tensile stress–strain curves of the $A_{35}P_5B_{17.5}M_{15}GO_{1.5}$ with maximum strain in the range of 100–500%, (D) 100%, (E) 200%, and (F) 500%, (G) compressive stress–strain curves of $A_{35}P_5B_{17.5}M_{15}GO_{1.5}$ for ten consecutive cycles, rheological scanning sweep of (H) frequency (I) strain sweep, (J) behavior of G' and G'' of the $A_{35}P_5B_{17.5}M_{15}GO_{1.5}$ as the shear strain between 1 and 300% in steps. (K) Tensile stress–strain curves of the $A_{35}P_5B_{17.5}M_{15}GO_{1.5}$ after healing at room temperature for 0.5 h, 1 h, 4 h, and 6 h, respectively, (L) strength and strain self-healing efficiency.

Subsequently, the hydrogel exhibited decreased elasticity and increased viscosity.

The self-healing performance of the nanocomposite hydrogel was investigated through oscillatory shear strain tests (Fig. 5J). Initially, a small-amplitude oscillatory shear strain of 1% was applied. Within the fixed intervals (33 s), the storage modulus (G') consistently remained higher than the loss modulus (G''), indicating the stability of the elastic network of the hydrogel under small strains. When the strain was increased to 300% (the breakdown point of 234%, as shown in Fig. 5I), both G' and G'' decreased significantly, with G'' becoming slightly higher than G', suggesting complete network disruption and a transition from gel to sol. Subsequently, when the strain was reduced back to 1%, G' and G'' almost returned to their original values, demonstrating rapid recovery capability. The hydrogel's ability to rapidly transition between the sol and gel states is attributed to the swift reconstruction of reversible borate ester bonds and numerous hydrogen bonds. These interactions endow the hydrogel with excellent self-healing properties, enabling it to promptly restore dynamic chemical cross-links after damage, thereby enhancing self-healing,

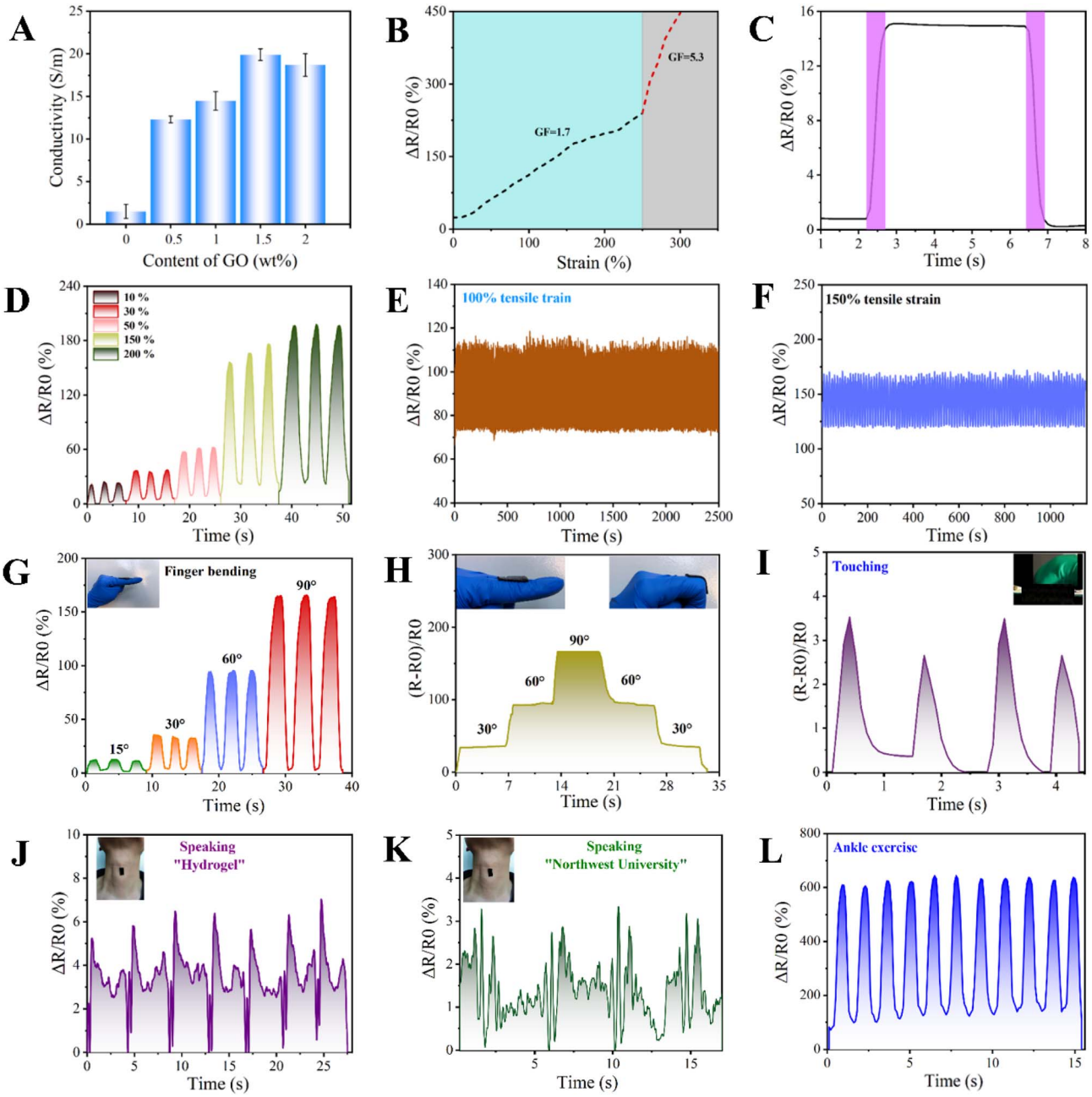

Fig. 6 Electric sensing property, (A) conductivity with different GO content, (B) GF at 0–300% strain, (C) response time, (D) relative resistance variation of various strains, (E) relative resistance variation at 1000 cycles of 100% tensile strain, (F) relative resistance variation at 100 cycles of 150% tensile strain, $A_{35}P_5B_{17.5}M_{15}GO_{1.5}$ hydrogel flexible sensor for human motion detection, relative resistance variation of (G) the continuous bending of fingers at different angles, (H) finger circular bending, (I) touch, (J) vocal cord recognition "Hydrogel" and (K) "Northwest University ", (L) ankle exercise.

ensuring structural stability, and maintaining overall integrity and functionality.

The self-healing efficiency of the composite hydrogels was quantitatively evaluated, and the results are presented in Fig. 5L. After the cross-section of the $A_{35}P_5B_{17.5}M_{15}GO_{1.5}$ sample underwent self-healing for a duration ranging from 0.5 h to 6 h, its fracture strength increased from 103.1 kPa to 144.3 kPa, and the elongation at break rose from 466% to 780% (Fig. 5K). Compared with the pristine hydrogel, the maximum strength self-healing efficiency (SE_σ) reached 89.1%, while the maximum strain self-healing efficiency (SE_ε) attained 83.1%.

As depicted in Fig. 5K, the fracture stress and strain of the healed $A_{35}P_5B_{17.5}M_{15}GO_{1.5}$ hydrogel increased significantly with the extension of healing time. This phenomenon demonstrates that when the hydrogel network constructed based on dynamic chemical bonds (*i.e.*, boronate ester bonds and hydrogen bonds) is damaged, the dynamic reversibility of boronate ester bonds and hydrogen bonds enables the network to rearrange

itself, thus endowing the hydrogel with excellent self-healing properties. The self-healing mechanism is illustrated in Fig. S5. Additionally, the rigid hydrogel building blocks interconnected *via* hydrogen bonding and van der Waals forces derived from graphene oxide (GO) exhibit dynamic characteristics. These components can effectively dissipate energy during deformation, which not only grants the hydrogel favorable elasticity and self-recovery capability but also enhances the structural stability of the network, ultimately contributing to the superior self-healing performance of the hydrogel.

2.6 Electrical and sensing performance

The $A_{35}P_5B_{17.5}M_{15}GO_{1.5}$ hydrogel exhibits strong self-healing ability and high stretchability, enabling it to closely conform to the human body. Its internal electronic conductive network brings new applications to flexible sensor technology. This hydrogel-based flexible sensor can rapidly respond to external stimuli and accurately detect minute pressures or strains, making it well-suited for monitoring various types of human movements. Fig. 6A demonstrates that electrical conductivity increases with increasing GO content, reaching a maximum at 1.5 wt%—a trend that can be quantitatively elucidated *via* electrical percolation theory. This conductivity evolution adheres to the classical percolation scaling law $\sigma = \sigma_0(\varphi - \varphi_c)^t$, where σ represents electrical conductivity, φ is the GO content, φ_c denotes the percolation threshold, and t stands for the critical exponent governing 3D network connectivity.

Increasing GO content promotes the connection of isolated GO nanosheets into a continuous electron-transport network. Conductivity rises sharply above the percolation threshold (estimated ~0.3–0.5 wt%) and peaks at 1.5 wt%, corresponding to an optimal conductive network with minimal contact resistance and homogeneous GO dispersion. Excess GO (>1.5 wt%) induces agglomeration, defects, and elevated tunneling barriers, resulting in reduced conductivity, consistent with typical behaviors of GO-based composites reported in ref. 42.

The estimated φ_c (~0.3–0.5 wt%) is consistent with the low percolation thresholds of GO/rGO polymer composites reported previously. The critical exponent $t \approx X$ (fitted from experimental data) matches 3D percolation theory ($t \approx$ 1.6–2.0), confirming the formation of a stable 3D conductive network in the composite.[43]

Fig. 6A illustrates the impact of GO content on the electrical conductivity of the flexible sensor: when 1.5 wt% GO is added, the sensor's electrical conductivity reaches 19.9 S m^{-1} without significant deterioration in mechanical properties. As the GO content increases, the electrical conductivity of the $A_{35}P_5B_{17.5}M_{15}GO_n$ series sensors initially rises markedly (specifically reaching 1.5, 12.3, 14.5, and 19.9 S m^{-1} at different GO levels), and then slightly decreases to 18.7 S m^{-1}. A high GO content leads to a slight reduction in electrical conductivity, and at 1.5 wt%, the GO is uniformly dispersed without aggregation.

The introduction of GO enhances the mechanical and self-healing properties of the flexible sensor, endowing it with good strain sensitivity (Gauge Factor, GF). As shown in Fig. 6B, the GF values are 1.7 and 5.3 in the strain ranges of 0–250% and 250–300%, respectively. Fig. 6C demonstrates that the flexible sensor also possesses rapid response capability (with a response time of 240 ms) and excellent signal stability. As depicted in Fig. 6D, the flexible sensor generates stable relative resistance changes under different tensile strains ranging from 10% to 200%. After undergoing 1000 cycles of 100% tensile strain and 100 cycles of 150% tensile strain, its output signal remains almost unchanged, indicating excellent cyclic performance (Fig. 6E and F).

When the flexible sensor is fixed on the finger joint, it can monitor in real-time the finger's motion as it bends from a straight position to different angles, such as 15°, 30°, 60°, and 90°. The changes in electrical signals are shown in Fig. 6G and H. During this process, the value of $\Delta R/R_0$ continuously increases with the increase in the bending angle, while also demonstrating repeatability and stability during reciprocal cycles at the same angle. In the field of flexible electronics, different bending angles can be distinguished by the value of $\Delta R/R_0$ to monitor joint motions at various angles.

In addition to joint motions, the flexible sensor also responds to slight pressures, as shown in Fig. 6I. When the sensor is gently touched by a finger, the relative resistance change is clearly recorded. When the flexible sensor is fixed on the throat, it can identify the relative resistance changes induced by spoken words (such as "Hydrogel" and "Northwestern University"), showing high repeatability (Fig. 6J and K). This characteristic may offer potential applications for human–machine interfaces and individuals with damaged vocal cords. Furthermore, when this "flexible electronic skin" is positioned on appropriate body parts, the flexible sensor can also monitor large-scale and rapid human motions. For example, when attached to the ankle (Fig. 6L), it can accurately respond to electrical signals generated during activities such as running.

3 Conclusions

In summary, graphene oxide (GO) was synthesized *via* the Hummers' method, and poly/(AM-*co*-AAPBA-PVA) hydrogels were fabricated by free radical polymerization. The preparation protocol was optimized to obtain the $A_{35}P_5B_{17.5}M_{15}$ hydrogel with superior mechanical strength and self-healing capabilities. Systematic studies were performed to elucidate the synergistic mechanism between borate ester bonds and nano-confinement-induced self-assembly, as well as their regulatory effects on the mechanical properties, self-healing efficiency, and sensing performances of the hydrogels. Subsequently, GO was utilized as a nano-reinforcer to prepare nano-confined graphene-based poly/(AM-*co*-AAPBA-PVA)/GO hydrogels. Experimental results revealed that the $A_{35}P_5B_{17.5}M_{15}$ hydrogel exhibited excellent mechanical self-healing properties, with a maximum stress of 161.6 kPa, breaking strain of 937%, elastic modulus of 151.0 kPa, and toughness of 107.6 MJ m^{-3}. After 6 h of self-healing, the recovery efficiencies of strength and strain reached 89.1% and 83.1%, respectively. The GO-confined hydrogel possessed dynamic features, favorable elasticity, as well as prominent self-recovery and self-healing performances. Moreover, this hydrogel showed remarkable fatigue resistance: it maintained a high

peak stress recovery rate after multiple tensile cycles under varying strains and remained undamaged even under high compressive strain. The $A_{35}P_5B_{17.5}M_{15}GO_{1.5}$ hydrogel achieved an electrical conductivity of 19.9 S m^{-1}, and the flexible sensor derived therefrom exhibited high sensitivity with a gauge factor (GF) of 5.3, a rapid response time of 240 ms, and stable cyclic performance over 1000 stretching cycles at 150% strain. Furthermore, the flexible sensor could accurately monitor various human activities, including joint flexion, finger bending, tactile perception, and vocal cord vibration. This work offers a promising strategy for the development of high-performance self-healing hydrogel-based flexible sensors, which hold great potential for applications in wearable electronics and human motion monitoring.

4 Experimental section

4.1 Materials

Acrylamide (AM, ≥99%, CAS 79-06-1), (3-acrylamidophenyl) boronic acid (AAPBA, ≥97%, CAS 99349-68-5), PVA (1799, polymerization degree 1700, MW ~78 000–82 000 g mol^{-1}, hydrolysis degree 98–99%, CAS 9002-89-5[7]) and MBA (≥99%, CAS 110-26-9[10]) were purchased from Aladdin Biochemical Technology Co., Ltd (Shanghai, China). GO was self-prepared.

4.2 Preparation of HPBA–GO hydrogels

4.2.1 Preparation of PVA solution. Deionized water was used to dissolve a predetermined amount of PVA, with continuous vigorous stirring at 90 °C for 1 hour; the resulting mixture was degassed by ultrasonication to yield the final polyvinyl alcohol solution.

4.2.2 Synthesis of composite hydrogel HPBA–GO. Initially, acrylamide (AM, 35 wt%), *N*,*N*′-methylenebisacrylamide (MBA, 1 mg mL^{-1}), and 3-acrylamidophenylboronic acid (AAPBA, 20 mg mL^{-1}) were dissolved in 2 mL of graphene oxide (GO) dispersion, followed by stirring at 850 rpm in 3 mL of 5 wt% polyvinyl alcohol (PVA) solution. After nitrogen purging for 30 min, 60 μL of ammonium persulfate (APS, 101 mg mL^{-1}) was added to the mixture. The resulting precursor solution was then injected into home-made cylindrical molds and incubated in an oven at 65 °C for 8 h to fabricate the composite hydrogel (designated as HPBA–GO; H = hydrogel, PB = AAPBA–PVA complex, PBA = P–B complex–AM copolymer, GO = graphene oxide).

4.3 Characterization methods

FTIR spectra were recorded on a Vertex70 (Bruker, Germany) in 4000–500 cm^{-1}. SEM (Quanta 450FEG-SEM, FEI, USA) was used to characterize the morphology of freeze-dried elastomers. XRD patterns were obtained with a Bruker D2 Phaser (Germany) under Cu Kα radiation (λ = 1.54 Å).

4.4 Mechanical tests

Mechanical properties were tested using a TA. XTC-18 tester (Shanghai BaoSheng, China). Tensile tests were conducted on columnar hydrogel specimens (length 20.0 mm, diameter 6.0 mm) at 50 mm min^{-1}. Cyclic compression tests were performed on cylindrical specimens (diameter 6 mm, height 10 mm) at 5 mm min^{-1} (room temperature) with a 60 s interval between cycles.

Tensile stress: $\sigma_t = F_t/\pi r^2$ (F_t: tensile force at strain t (N); r: original radius (mm)).

Tensile strain: $\varepsilon_R = [(L_R - L_0)/L_0] \times 100\%$ (L_R: grip displacement; L_0: initial length).

Tensile strength (σ_b) and elongation at break (ε_b) refer to stress and strain at specimen fracture.

4.5 Self-healing tests

Self-healing efficiency (SE) was quantified *via* tensile/compression tests using a TA. XTC-18 tester. Cylindrical elastomer specimens (length 25.0 mm, diameter 6.0 mm) were cut into two halves, and the cut surfaces were contacted without external pressure (sealed to prevent water evaporation). Stretchability of $A_{35}P_5B_{17.5}M_{15}GO_{1.5}$ was tested after healing for 0.5 h, 1 h, 4 h and 6 h.

$SE_\sigma = \sigma_s/\sigma_o \times 100\%$, $SE_\varepsilon = \varepsilon_s/\varepsilon_o \times 100\%$ (σ_s, ε_s: stress/strain of healed specimen; σ_o, ε_o: stress/strain of original specimen).

4.6 Rheological measurements

Rheological behavior of $A_{35}P_5B_{17.5}M_{15}GO_{1.5}$ was analyzed using an MCR 302 rheometer (Anton Paar, China) with round specimens (thickness 1 mm, diameter 25 mm). Strain scan: 0.1–1000% strain, 10 rad s^{-1} frequency. Step strain sweep: 10 rad s^{-1} frequency, strain 1–300% (strain failure). All self-healing experiments were conducted at room temperature unless stated otherwise.

4.7 Electrical and sensing performances

Electrical conductivities were measured using an Autolab electrochemical workstation (Aptar, Switzerland). Sensing performance for human activities (finger, wrist, knee, throat movements) was tested by placing the elastomer at the corresponding positions.

Relative resistance: $\Delta R/R_0 = (R - R_0)/R_0 = (I_0 - I)/I$ (I_0, I: initial and real-time currents; R, R_0: resistances with/without strain).

Gauge factor (GF): $GF = (R - R_0)/(R_0 \times \varepsilon)$ (ε: strain).

Conductivity (σ, S m^{-1}): $\sigma = d/(R \times A)$ (d: electrode distance; R: impedance; A: cross-sectional area), measured *via* AC impedance (10^{-1}–10^6 Hz).

Sensor dimensions: 60 mm × 10 mm × 2 mm (length × width × thickness) for all sensing tests.

Other specific methods are in the SI (4.3–4.7).

Author contributions

Lili Tian: first writing, data analysis, software, writing – original draft preparation. Zhiming Yang: investigation, methodology. Qin Wang: visualization and data curation.

Conflicts of interest

The authors declare that they have no known competing financial interests or personal relationships that could have appeared to influence the work reported in this paper.

Data availability

All data underpinning the study conclusions are presented in the main text. Comprehensive details, including experimental protocols, characterization techniques and self-healing mechanism, are provided in the supplementary information (SI). Supplementary information is available. See DOI: https://doi.org/10.1039/d6ra01645f.

Acknowledgements

This work was financially funded by the Research Program of Ningxia Key Laboratory of Green Catalytic Materials and Technology (2025SYSYB-22), Ningxia Natural Science Foundation (2026A0681), Guyuan Municipal Research and Development Science and Technology Program Project (2024BGTYF01-50, 2025GKJYF0018).

References

1 Y. Tian, Z. H. Wang, S. Y. Cao, D. Liu, Y. K. Zhang, C. Chen, Z. W. Jiang, J. Ma and Y. L. Wang, *Nat. Commun.*, 2024, **15**, 10.
2 L. L. Tian, T. S. Liu, Y. X. Jiang, B. Y. He and H. Hao, *Chem. Eng. J.*, 2024, **497**, 11.
3 Y. Cheng, M. M. Hu, J. Cao, H. Zhang, X. Y. Ma, Y. J. Wu and J. T. Guo, *J. Colloid Interface Sci.*, 2025, **693**, 13.
4 J. P. Zhang, J. H. Zou and J. N. Ren, *Front. Bioeng. Biotechnol.*, 2025, **13**, 30.
5 B. W. Guo, Z. K. Wang, L. Zheng, G. Mo, H. J. Zhou and D. Luo, *Carbon Energy*, 2024, **6**, 16.
6 M. F. Lu, Z. H. Gu, K. Feng, Y. L. Gao and Z. X. Jin, *ACS Sustain. Chem. Eng.*, 2022, **10**, 3007–3015.
7 S. W. Wang, Y. Y. Ma, S. L. Zhu, H. Y. Ma, Y. Y. Yue, Q. L. Wu, H. N. Xiao and J. Q. Han, *Chem. Eng. J.*, 2024, **495**, 12.
8 Z. K. Li, B. Wang, J. J. Lu, Y. M. Xue, J. X. Wang, B. Q. Jia, G. Y. Han, Y. H. Zhao, M. A. K. Qureshi, L. Yu, K. Zhao, M. Li, P. Yang, D. J. Lu and L. B. Zhao, *Adv. Sci.*, 2025, **12**, 13.
9 J. X. Zhang, X. W. Shi, Z. T. Zhao, M. Y. Wang, H. B. Deng and Y. M. Du, *Adv. Sci.*, 2024, **11**, 11.
10 M. Babaluei, Y. Mojarab, F. Mottaghitalab and M. Farokhi, *Int. J. Biol. Macromol.*, 2023, **249**, 19.
11 B. X. Xue, Z. Y. Shao, J. Liu, Y. Liu, M. Niu, Y. Z. Yang and L. Zhang, *Int. J. Biol. Macromol.*, 2025, **311**, 13.
12 L. L. Tian, B. Y. He, Y. L. Liu, Q. Zhang, S. S. Liang, Y. H. Yuan, Q. Han, S. C. Ju, L. Y. Cong, C. Y. Cai and H. Hao, *ACS Appl. Polym. Mater.*, 2024, **6**, 9099–9109.
13 X. M. Li, W. J. Xu, Y. Xin, J. W. Yuan, Y. C. Ji, S. N. Chu, J. Q. Liu and Q. Luo, *Polymers*, 2021, **13**, 17.
14 N. Manousi, E. Rosenberg, E. Deliyanni, G. A. Zachariadis and V. Samanidou, *Molecules*, 2020, **25**, 22.
15 Q. H. Yang, Z. M. He, Y. L. Shi, J. X. Wang, Q. Y. Qiu, H. H. Deng and W. H. Ping, *Chin. J. Anal. Chem.*, 2024, **52**, 8.
16 A. S. Gubin, P. T. Sukhanov and A. A. Kushnir, *J. Anal. Chem.*, 2025, **80**, 198.
17 C. Huang, W. H. Feng, S. Y. Hou, Z. D. Jiang, Y. X. Wu, Y. Z. Wang, D. W. Ding, S. S. Gao, F. R. Li, X. Z. Zhao, P. A. Hu and Y. L. Pan, *Chem. Eng. J.*, 2025, **520**, 11.
18 C. Huang, W. S. Yang, H. Wang, S. C. Huang, S. S. Gao, D. L. Li, J. L. Liu, S. Y. Hou, W. H. Feng, Z. R. Wang, F. R. Li, Z. Hao, X. Z. Zhao, P. A. Hu and Y. L. Pan, *ACS Nano*, 2024, **18**, 21198–21210.
19 C. Zhang, Q. T. Lai, W. Chen, Y. K. Zhang, L. Mo and Z. C. Liu, *Biosensors*, 2023, **13**, 28.
20 X. Liu, T. Wei, J. Englhard, M. Barr, A. Hirsch and J. Bachmann, *Adv. Sci.*, 2025, **12**, 7.
21 L. A. Jiang, S. Tian, Y. H. Xie, X. Lv and S. L. Sun, *Langmuir*, 2023, **39**, 8698–8709.
22 Y. Yang, C. Yao, W. Y. Huang, C. L. Liu and Y. Zhang, *ACS Appl. Mater. Interfaces*, 2024, **16**, 11957–11972.
23 Y. C. Li, S. Z. Tan, X. S. Zhang, Z. Y. Li, J. Cai and Y. N. Liu, *Gels*, 2025, **11**, 27.
24 Y. B. Luo, J. Y. Li, Q. L. Ding, H. Wang, C. Liu and J. Wu, *Nano-Micro Lett.*, 2023, **15**, 45.
25 B. S. Yin, F. R. Liu, Q. Y. Chen, M. Liu and F. Y. Wang, *Sensors*, 2024, **24**, 13.
26 G. Rando, E. Scalone, S. Sfameni and M. R. Plutino, *Gels*, 2024, **10**, 43.
27 X. Luo, H. D. Tan and W. J. Wen, *Bioengineering*, 2024, **11**, 31.
28 Y. Q. Liu, Z. Y. Li, C. F. Zhang, B. R. Yang and H. Ren, *Polymers*, 2023, **15**, 12.
29 K. Chen, H. M. Xie and J. Liu, *Polym. Chem.*, 2024, **15**, 2370–2376.
30 B. Q. Jin, W. Q. Wu and H. T. Wu, *Polymers*, 2023, **15**, 11.
31 R. Abouzeid, M. Shayan, T. Y. Wu, J. Gwon, T. A. Kärki and Q. L. Wu, *ACS Appl. Polym. Mater.*, 2023, **5**, 7009–7021.
32 X. K. Guo, S. L. Zhang, S. Patel, X. L. Sun, Y. L. Zhu, Z. C. Wei, R. G. Wang, X. D. He, Z. K. Wang, C. J. Yu and S. C. Tan, *Sci. Adv.*, 2025, **11**, 14.
33 S. H. Lee, S. Yoo, S. H. Kim, Y. M. Kim, S. I. Han and H. Lee, *Mater. Today Bio*, 2025, **31**, 21.
34 A. M. Soomro, B. Jawed, A. Qayoom, H. Hyder, K. Hussain, L. Iram, M. Waqas, F. Ahmed, A. Sattar, S. Almani and J. H. Lim, *Phys. Status Solidi A*, 2024, **221**, 29.
35 S. Wang, H. R. Zhai, Q. Zhang, X. L. Hu, Y. J. Li, X. Xiong, R. H. Ma, J. L. Wang, Y. Chang and L. X. Wu, *Nanomaterials*, 2025, **15**, 35.
36 J. X. Dong, X. R. Yang, J. H. Li and H. Z. Liu, *Int. J. Biol. Macromol.*, 2025, **322**, 10.

37 X. Gao, C. F. Yan, Y. T. Wang, W. Y. Wang, C. Chang, H. C. Zhang, Y. A. Wang, J. M. Cao, X. Duan, S. Y. Yu, C. H. Linghu, J. Park and J. Wu, *J. Colloid Interface Sci.*, 2026, **706**, 13.
38 Y. Wan, X. C. Li, H. T. Yuan, D. X. Liu and W. Y. Lai, *Adv. Funct. Mater.*, 2024, **34**, 29.
39 C. Chen, T. Shen, J. Yang, W. K. Cao, J. H. Wei and W. H. Li, *Chem. Eng. J.*, 2024, **498**, 19.
40 L. Y. Cong, W. Z. Liu, L. L. Tian, C. Y. Cai, Q. Han, S. C. Ju, Y. L. Zhao, Q. Zhang and H. Hao, *Polym. Eng. Sci.*, 2025, **65**, 2258–2267.
41 S. Kumar, R. Singh and N. S. Maurya, *Environ. Sci. Pollut. Res.*, 2023, **30**, 45428–45444.
42 X. W. Zhu, Q. Y. Gao, M. M. Lou, Y. Bai, X. M. Xu, F. Li and B. van der Bruggen, *J. Membr. Sci.*, 2024, **707**, 11.
43 J. H. Tang, B. X. Yang, T. Duanmu, Z. P. Mao and J. Zhang, *Polym. Compos.*, 2024, **45**, 8065–8075.